



Article

# Visible Light Driven Photoanodes for Water Oxidation Based on Novel r-GO/ $\beta$ -Cu<sub>2</sub>V<sub>2</sub>O<sub>7</sub>/TiO<sub>2</sub> Nanorods Composites

Shuang Shuang<sup>1,2,3,†</sup> , Leonardo Girardi<sup>1,†</sup>, Gian Andrea Rizzi<sup>1,\*</sup> , Andrea Sartorel<sup>1</sup> ,  
Carla Marega<sup>1</sup>, Zhengjun Zhang<sup>3</sup> and Gaetano Granozzi<sup>1</sup>

<sup>1</sup> University of Padova and INSTM Unit, via Marzolo 1, 35121 Padova, Italy; shuangshuang\_buct@163.com (S.S.); leonardo.girardi@phd.unipd.it (L.G.); andrea.sartorel@unipd.it (A.S.); carla.marega@unipd.it (C.M.); gaetano.granozzi@unipd.it (G.G.)

<sup>2</sup> State Key Laboratory of New Ceramics and Fine Processing, School of Materials Science and Engineering, Tsinghua University, Beijing 100084, China

<sup>3</sup> Key Laboratory of Advanced Materials (MOE), School of Materials Science and Engineering, Tsinghua University, Beijing 100084, China; zjzhang@mail.tsinghua.edu.cn

\* Correspondence: gianandrea.rizzi@unipd.it; Tel.: +39-049-827-5722

† These authors contributed equally to this work.

Received: 4 June 2018; Accepted: 16 July 2018; Published: 18 July 2018



**Abstract:** This paper describes the preparation and the photoelectrochemical performances of visible light driven photoanodes based on novel r-GO/ $\beta$ -Cu<sub>2</sub>V<sub>2</sub>O<sub>7</sub>/TiO<sub>2</sub> nanorods/composites.  $\beta$ -Cu<sub>2</sub>V<sub>2</sub>O<sub>7</sub> was deposited on both fluorine doped tin oxide (FTO) and TiO<sub>2</sub> nanorods (NRs)/FTO by a fast and convenient Aerosol Assisted Spray Pyrolysis (AASP) procedure. Ethylenediamine (EN), ammonia and citric acid (CA) were tested as ligands for Cu<sup>2+</sup> ions in the aerosol precursors solution. The best-performing deposits, in terms of photocurrent density, were obtained when NH<sub>3</sub> was used as ligand. When  $\beta$ -Cu<sub>2</sub>V<sub>2</sub>O<sub>7</sub> was deposited on the TiO<sub>2</sub> NRs a good improvement in the durability of the photoanode was obtained, compared with pure  $\beta$ -Cu<sub>2</sub>V<sub>2</sub>O<sub>7</sub> on FTO. A further remarkable improvement in durability and photocurrent density was obtained upon addition, by electrophoretic deposition, of reduced graphene oxide (r-GO) flakes on the  $\beta$ -Cu<sub>2</sub>V<sub>2</sub>O<sub>7</sub>/TiO<sub>2</sub> composite material. The samples were characterized by X-ray Photoelectron Spectroscopy (XPS), Raman, High Resolution Transmission Electron Microscopy (HR-TEM), Scanning Electron Microscopy (SEM), Wide Angle X-ray Diffraction (WAXD) and UV-Vis spectroscopies. The photoelectrochemical (PEC) performances of  $\beta$ -Cu<sub>2</sub>V<sub>2</sub>O<sub>7</sub> on FTO,  $\beta$ -Cu<sub>2</sub>V<sub>2</sub>O<sub>7</sub>/TiO<sub>2</sub> and r-GO/ $\beta$ -Cu<sub>2</sub>V<sub>2</sub>O<sub>7</sub>/TiO<sub>2</sub> were tested in visible light by linear voltammetry and Electrochemical Impedance Spectroscopy (EIS) measurements.

**Keywords:** copper vanadate; photoanode; water splitting; graphene oxide

## 1. Introduction

The hydrogen economy is a new intriguing sustainable scenario, and it is expected that sooner or later it is going to replace the hydrocarbon economy [1]. With this perspective, a worldwide goal is to provide sustainable and convenient methods to prepare hydrogen fuel. Among them, water splitting (WS), by exploiting the energy of sun, is the most appealing, and many different approaches are currently being investigated [2]. The advantage of the photoelectrochemical (PEC) approach, compared to the standard photocatalytic one, is that an external potential is used to facilitate the WS process. The intrinsic simplicity of PEC, which combines the light absorber and the energy converter into a single device capable to store solar energy into chemical bonds, is rather evident. For these reasons, numerous studies have been performed to fabricate semiconducting nanomaterials with

enhanced PEC properties under visible light. In particular, many efforts have been done on developing materials for photoanodes, where the kinetically hindered Oxygen Evolution Reaction (OER) is occurring. Their final performance depends upon the electrocatalysts stability against oxidation [3] and on their intrinsic band energetics [4].

Metal oxide semiconductors are promising photoanode materials because of their relative stability to oxidative photo-corrosion and their low-cost. Hematite, ( $\alpha$ -Fe<sub>2</sub>O<sub>3</sub>), has been identified as an efficient photoanode material characterized by a sufficiently low band gap of 1.9–2.0 eV, to be used as “top” electrode in a “tandem” WS device [5]. Nevertheless, this material has some shortcomings, such as a short carrier diffusion length, a significant recombination and indirect absorption. During the last few years, other multicomponent oxides have been suggested as possible active materials for the construction of photoanodes. Among them, ZnFe<sub>2</sub>O<sub>4</sub>, CuWO<sub>4</sub>, CuW<sub>1-x</sub>Mo<sub>x</sub>O<sub>4</sub> and especially Cu-vanadates are particularly studied. As with many transition metal (TM) vanadates, Cu-vanadates are characterized by different phases where the Cu/V ratio has a quite large variability. The performances of these phases, together with their PEC stability, were tested in a very comprehensive paper by Gregoire et al. [6]. In their study it was shown that sputter-deposited phases having lower Cu/V ratios are less stable, in borate buffer solution (pH = 9.2), than other phases with higher Cu/V ratio, (e.g.,  $\gamma$ -Cu<sub>3</sub>V<sub>2</sub>O<sub>8</sub> and Cu<sub>11</sub>V<sub>6</sub>O<sub>26</sub>). The  $\gamma$ -Cu<sub>3</sub>V<sub>2</sub>O<sub>8</sub> based photoanodes, prepared by sol-gel method were also recently studied by Neale et al. [7]. The results of these studies were that the V-rich phases suffered from V loss and a consequent decay in the PEC properties, while the higher stability of Cu rich phases was attributed to a self-passivating mechanism that led to the formation of Cu<sup>+</sup> and Cu<sup>2+</sup> oxides on the vanadate surface. In a successive study, again by Gregoire et al. [4], a library of Cu-vanadates thin films with variable stoichiometry was prepared by a fast and convenient ink-jet printing procedure and, again, it resulted that both  $\alpha$ -CuV<sub>2</sub>O<sub>6</sub> and  $\alpha$ -Cu<sub>2</sub>V<sub>2</sub>O<sub>7</sub> are highly active and stable photocatalysts in a borate buffer solution, while  $\beta$ -Cu<sub>2</sub>V<sub>2</sub>O<sub>7</sub> demonstrated a high photoelectroactivity in the presence of ferri/ferrocyanide redox couple at pH = 13. The abovementioned phases,  $\alpha$ -CuV<sub>2</sub>O<sub>6</sub> and  $\beta$ -Cu<sub>2</sub>V<sub>2</sub>O<sub>7</sub> were also deposited by a simple drop casting method on fluorine doped tin oxide (FTO) glass and their PEC properties characterized by Mullins et al. [8]. This study showed that the V rich  $\alpha$ -CuV<sub>2</sub>O<sub>6</sub> phase is the one showing the highest photocurrent, although both phases were characterized by a short diffusion length for holes and required the addition of a hole scavenger like Na<sub>2</sub>SO<sub>3</sub> to improve the photocurrent density. Finally, in a more recent paper by Sharp et al. [9] it was shown that, although Cu-rich phases show higher absorption and charge separation, these phases also present a higher surface recombination rate. Therefore, considering that Cu-rich phases are the ones showing the higher stability in borate buffer solutions, good charge separation and higher absorption and that, on the other hand, V rich phases seem to be those characterized by the higher photocurrents density, we decided to concentrate our attention on the  $\beta$ -Cu<sub>2</sub>V<sub>2</sub>O<sub>7</sub> phase, that appeared to be a good compromise between durability and PEC performances. The idea of increasing the adhesion between the substrate and the vanadate particles, in order to improve the durability in the electrolyte solution, led us to think about the use of a high surface area substrate like TiO<sub>2</sub> nanorods (NRs) on FTO [10], to grow this n-type semiconductor. Moreover, the addition of graphene oxide (GO) flakes, could lead to the formation of a composite material with interesting PEC proprieties in term of durability and photocurrent density. In fact, quite recently, composite systems like BiVO<sub>4</sub>/TiO<sub>2</sub> and V<sub>2</sub>O<sub>5</sub>/BiVO<sub>4</sub>/TiO<sub>2</sub> were prepared by hydrothermal synthesis and, although not used as active material in photoanodes, showed superior photocatalytic performances in the degradation of organics caused by an upward shift of V<sub>2</sub>O<sub>5</sub> and BiVO<sub>4</sub> conduction bands with respect to TiO<sub>2</sub> with formation of an n-n junction [11,12]. A similar approach was also used by Chen and coworkers [13] where TiO<sub>2</sub> NRs were decorated by Fe<sub>2</sub>O<sub>3</sub> grown on preformed TiO<sub>2</sub> NRs obtained by a simple hydrothermal synthesis. With respect to the effect of the addition of GO flakes, it is useful to remind that GO and especially partial reduced GO (r-GO), are considered as a good support for nanostructures because of their carrier mobility [14], large specific area and high optical transmittance [15,16]. Moreover, when TiO<sub>2</sub> nanostructures are combined with GO or r-GO

they usually can shuttle and store more electrons due to the formation of many p-n nanojunctions with r-GO, a p-type semiconductor [17–19].

In this study, we describe the preparation and evaluation of the PEC performances of a visible light driven photoanode based on a novel composite material consisting on  $\beta$ - $\text{Cu}_2\text{V}_2\text{O}_7$  nanoparticles deposited on  $\text{TiO}_2$  NRs followed by the addition of r-GO flakes. The decoration of  $\text{TiO}_2$  NRs with  $\beta$ - $\text{Cu}_2\text{V}_2\text{O}_7$  NPs was obtained by an easy and fast aerosol assisted spray pyrolysis (AASP) deposition technique. A further improvement of the performances was obtained by the addition of partially reduced graphene oxide (r-GO), a p-type semiconductor [20], to reduce the charge transfer resistance. We show here that GO, deposited by electrophoretic deposition, can efficiently coat the surface of the  $\beta$ - $\text{Cu}_2\text{V}_2\text{O}_7/\text{TiO}_2$  nanostructures and, after a mild annealing, is transformed into r-GO causing a remarkable enhancement of the photocurrent with increased durability (from  $50 \mu\text{A}/\text{cm}^2$  in the case of pure  $\text{TiO}_2$  NRs,  $150 \mu\text{A}/\text{cm}^2$  for  $\text{TiO}_2$  NRs decorated with  $\beta$ - $\text{Cu}_2\text{V}_2\text{O}_7$  NP to  $250 \mu\text{A}/\text{cm}^2$  for r-GO/ $\beta$ - $\text{Cu}_2\text{V}_2\text{O}_7/\text{TiO}_2$ ).

The prepared films were characterized by wide angle X-ray diffraction (WAXD), scanning electron microscopy (SEM), high resolution transmission electron microscopy (HR-TEM), UV–Vis and Raman spectroscopy, Electrochemical Impedance Spectroscopy (EIS) and PEC measurements. Their surface composition was also studied by X-ray Photoemission Spectroscopy (XPS) before and after the PEC work, under illumination, with the intention of verifying V loss and concomitant formation of  $\text{CuO}_x$  passivating layers.

## 2. Materials and Methods

### 2.1. Material Preparation

All the reagents used in this study were analytical grade and purchased from Sigma-Aldrich (Milan, Italy). The photoactive material of this study,  $\beta$ - $\text{Cu}_2\text{V}_2\text{O}_7$  was deposited on FTO or FTO/ $\text{TiO}_2$  substrates by a quick and convenient AASP method. This method consisted of the evaporation of a precursor solution micro-droplets onto a heated substrate. The micro-droplets were produced by the nebulization created through ultrasounds. Using a stream of gas (i.e., air), the micro droplets were transported near the substrate. Malachite [ $\text{Cu}_2(\text{OH})_2\text{CO}_3$ ] was used as a copper-source for the aerosol solution because it contains “clean” anionic groups (carbonate and hydroxide) that do not introduce other contamination into the solution. For the preparation of  $\text{Cu}_2(\text{OH})_2\text{CO}_3$ , potassium hydrogen carbonate (10.0 g, 100 mmol) and copper sulphate pentahydrate (10.0 g, 40 mmol) were dissolved in 150 mL of hot water within two beakers. The two solutions were mixed together after being cooled. Immediately, a teal blue precipitate formed. These precipitates were recovered by “Büchner” filtration and washed with water and ethanol. The reaction that takes place is:



The solid was dried on a hot plate at ca.  $200^\circ\text{C}$ ; this was because at a temperatures close to  $300^\circ\text{C}$ , malachite starts to decompose [21]. The aerosol precursor solution was prepared using a malachite suspension in water followed by the addition of a suitable ligand to complex  $\text{Cu}^{2+}$  ions, thus preventing the direct precipitation of copper vanadate, once the vanadate source is added. After complete dissolution of the malachite suspension, the vanadium-source ( $\text{NH}_4\text{VO}_3$ ) was added. Ammonia, citric acid (CA) and ethylenediamine (EN) were used as ligands to prepare precursor solutions 1, 2 and 3, respectively.

**Solution 1**  $\text{Cu}_2(\text{OH})_2\text{CO}_3$  (0.23 g, 1 mmol) was added to 10 mL of deionized water followed by the addition of 2 mL of concentrated (33%)  $\text{NH}_3$  solution, under vigorous stirring. Ammonium vanadate,  $\text{NH}_4\text{VO}_3$  (0.25 g, 2 mmol), was added until a clear solution was formed.

**Solution 2** CA (0.63 g, 3 mmol) and malachite (0.23 g, 1 mmol) were dissolved in 10 mL of deionized water. Ammonium vanadate (0.25 g, 2 mmol) was added to this solution.

**Solution 3** EN (150  $\mu\text{L}$ , 2 mmol) and, malachite (0.23 g, 1 mmol) were dissolved in 10 mL of deionized water. Ammonium vanadate (0.25 g, 2 mmol) was added to this solution.

TiO<sub>2</sub> NRs were fabricated on FTO glass (TiO<sub>2</sub>/FTO) by the hydrothermal method [22]. 2 FTO slides (1 cm  $\times$  1.5 cm  $\times$  0.2 cm) were cleaned with isopropanol and deionized water in a sonicator for 30 min. The precursor solution was prepared by combining 3.44 mL of deionized water with 3.44 mL of HCl 37% and mixing for 10 min. Finally, 120  $\mu\text{L}$  of titanium isopropoxide [Ti(OCH(CH<sub>3</sub>)<sub>2</sub>)<sub>4</sub>] were added under vigorous stirring. This solution was poured into the Teflon-liner with the FTO substrates together. The whole system was heated to 150 °C for 4 h and cooled down to room temperature (RT), after extraction from the oven. The FTO slides were finally rinsed with abundant deionized water.

Deposition of copper vanadate, either on clean FTO or on TiO<sub>2</sub> NRs, was carried out using a commercial aerosol medical device (Artsana Projet). To avoid ammonia evaporation, in the case of solution 1, an excess of ammonia water solution was used (4 mL of solution 1 and 2 mL of 33% ammonia water solution).

The aerosol was conveyed through a tube (flow rate of about 60 mL/min) to a funnel neck, just above the substrate that was positioned on a metal plate heated by a Boraelectric heater (Tectra, GmbH, Frankfurt, Germany), connected to a power supply. A K-type thermocouple was positioned between the plate and the heater, to have accurate control of the sample temperature. The substrate was heated for 20 min to 340 °C. During the deposition the temperature decreased to 320 °C. The optimal deposition time on FTO was found to be 5 min, while on TiO<sub>2</sub>/FTO, the best results were obtained after 3 min. The TiO<sub>2</sub>/FTO and the  $\beta\text{-Cu}_2\text{V}_2\text{O}_7/\text{FTO}$  samples were then annealed in air at 450 °C for 2 and 4 h, respectively.

GO was synthesized from graphite using an Improved Hummers' method [23], developed from Marcano et al.; GO water suspension (2.5 mg/mL; pH = 6.5) was prepared using a sonicator to disperse the flakes.

The deposition was carried out by an electrophoretic process (2.5 mg/mL GO water suspension, pH = 6.5). A 5V potential was applied for 30 s between the sample (positive pole) and a clean FTO glass. The FTO slides were separated by a distance of 1.5 cm. After the deposition, the sample was annealed in air at 200 °C for 15 min.

## 2.2. Material Characterization

The morphology and nanostructure of all samples were characterized by field-emission gun SEM (Zeiss Supra 35VP, Zeiss, Jena, Germany) and High-Resolution TEM (JEOL-2011, JEOL Ltd., Tokyo, Japan). Surface composition was determined by XPS measurements performed on a custom-built UHV chamber (base pressure =  $5 \times 10^{-10}$  mbar) equipped with a non-monochromatized double-anode X-ray source (Omicron DAR-400, Scienta-Omicron GmbH, Uppsala, Sweden), a hemispherical electron analyzer (Omicron EA-125, Scienta-Omicron GmbH, Uppsala, Sweden) and a 5-channeltrons detection assembly. The electron analyzer had an acceptance angle of  $\pm 4^\circ$  and the diameter of the analyzed area was 3 mm. The spectra were acquired with Al-K $\alpha$  radiation. WAXD patterns were recorded in the diffraction angular range 10–50° 2 $\theta$  by a Philips X'Pert PRO diffractometer, working in the reflection geometry and equipped with a graphite monochromator on the diffracted beam (CuK $\alpha$  radiation, Pananalytical, Almelo, The Netherlands). Raman spectra were acquired with a Thermo-Fisher DXR Raman microscope using a 532 nm laser (5 mW), focused on the sample with a 50 $\times$  objective (Thermo-Fisher Scientific, Madison, WI, USA) obtaining a spot size of about 1  $\mu\text{m}$ . UV-Vis spectra were acquired in absorbance and reflectance mode on a UV-Vis Cary 5E spectrophotometer.

All the electrochemical measurements were obtained in a Na borate buffer solution prepared adding NaOH to a 0.4 M solution of boric acid until pH = 9.2 was reached (example of PEC measurement obtained in Na-sulphate solution reported in Figures S1 and S2). The measurements were made in a Teflon PEC cell (see Figure S3). A Pt wire and Ag/AgCl electrode were used as counter electrode and reference electrode, respectively. PEC measurements were obtained by a visible light emitting diode (LED) source (see Figure S4) controlled by the optical bench (Metrohm-Autolab)

coupled to the Autolab PGSTAT204 (Metrohm, Utrecht, The Netherlands) instrument. The samples were mounted outside the cell and kept in position by an O-ring seal. All samples were illuminated from the back side (comparison between front-side and back-side illumination reported in Figure S5) and the electrical contact was obtained by a Cu strip attached to the FTO glass surface by Silver Conductive Paint (RS). EIS data were obtained under illumination and in the dark at 1.75 V vs. Reversible Hydrogen Electrode (RHE). The amplitude for EIS measurements was  $\pm 10$  mV with the frequency range set from  $10^5$  to  $10^{-1}$  Hz, performing 50 points with logarithmic distribution. Oxygen measurement was carried out by NEOFOX-KIT PROBE from Ocean Optics (Ocean Optics, 8060 Bryan Dairy Rd, Largo, FL 33777, USA).

### 3. Results and Discussion

The PEC measurements on  $\beta$ - $\text{Cu}_2\text{V}_2\text{O}_7$  films deposited on FTO ( $\beta$ - $\text{Cu}_2\text{V}_2\text{O}_7$ ) using different aerosol solutions (solution 1–3) are discussed later in the text, nevertheless, it is useful to anticipate that vanadates prepared using solution 1 ( $\text{NH}_3$ ) gave the best PEC results with respect to the other two solutions. For this reason, only  $\beta$ - $\text{Cu}_2\text{V}_2\text{O}_7$  on  $\text{TiO}_2$  NRs ( $\beta$ - $\text{Cu}_2\text{V}_2\text{O}_7/\text{TiO}_2$ ) and r-GO/ $\beta$ - $\text{Cu}_2\text{V}_2\text{O}_7$  on  $\text{TiO}_2$  (r-GO/ $\beta$ - $\text{Cu}_2\text{V}_2\text{O}_7/\text{TiO}_2$ ) samples, obtained with solution 1 (see experimental section) are herein discussed. We attributed this behavior to a lower carbon contamination.

Figure 1a shows the Raman spectra of  $\beta$ - $\text{Cu}_2\text{V}_2\text{O}_7$ ,  $\text{TiO}_2$ ,  $\beta$ - $\text{Cu}_2\text{V}_2\text{O}_7/\text{TiO}_2$  and r-GO/ $\beta$ - $\text{Cu}_2\text{V}_2\text{O}_7/\text{TiO}_2$ , measured at room-temperature. The Raman region of pure  $\text{TiO}_2$  NRs presents all the characteristic peaks corresponding to rutile, that is, the peak at  $244\text{ cm}^{-1}$  corresponding to the phonon scattering mode of rutile, the signal at  $438\text{ cm}^{-1}$  assigned to the  $E_g$  mode, and the peak at  $621\text{ cm}^{-1}$  to the  $A_{1g}$  mode [24]. The peak centered at  $914\text{ cm}^{-1}$  is the characteristic band assigned to the  $\beta$ - $\text{Cu}_2\text{V}_2\text{O}_7$  ( $\text{VO}_3$  stretching mode) [25]. In the case of r-GO/ $\beta$ - $\text{Cu}_2\text{V}_2\text{O}_7/\text{TiO}_2$  NRs sample, two broad peaks at  $1354$  ( $I_D$ ) and  $1598\text{ cm}^{-1}$  ( $I_G$ ) are those characteristic of r-GO [26]. In particular, the  $I_D/I_G$  ratio corresponding to thick r-GO flakes was 0.97, as reported in reference [26], while in the case of areas where the r-GO coating was not visible by the micro-Raman microscope ( $50\times$ ), the ratio was 0.89 before PEC measurements and was reduced to 0.85 after PEC measurements (see Supplementary Material, Figure S6). These values are completely consistent with the presence of r-GO. Figure 1b shows the WAXD patterns of the prepared samples:  $\beta$ - $\text{Cu}_2\text{V}_2\text{O}_7$ ,  $\beta$ - $\text{Cu}_2\text{V}_2\text{O}_7/\text{TiO}_2$ , and r-GO/ $\beta$ - $\text{Cu}_2\text{V}_2\text{O}_7/\text{TiO}_2$ . The diffraction peak at  $2\theta = 24.7^\circ$  (cyan curve) is assigned to reflections from planes (200) of monoclinic  $\beta$ - $\text{Cu}_2\text{V}_2\text{O}_7$  (JCPDS No. 73-1032), while peaks at  $2\theta = 36.2^\circ$  and  $62.9^\circ$  (red, green and blue curves) correspond to reflections from planes (101) and (002) of rutile (JCPDS No. 21-1276). We calculated the lattice parameters of  $\text{TiO}_2$ -rutile NRs before and after the coating with  $\text{Cu}_2\text{V}_2\text{O}_7$ . These parameters are:  $a = 4.569(9)\text{ \AA}$ ,  $c = 2.955(2)\text{ \AA}$ , remaining unchanged after the coating. The blue curve (r-GO/ $\beta$ - $\text{Cu}_2\text{V}_2\text{O}_7/\text{TiO}_2$ ) presents a further diffraction peak, at  $2\theta = 24.7^\circ$ , that has to be attributed to r-GO [27].

Indeed, the XRD pattern of  $\beta$ - $\text{Cu}_2\text{V}_2\text{O}_7/\text{TiO}_2$  (green curve) shows an extremely weak peak at  $2\theta = 24.7^\circ$ . However, the very low intensity of this peak, probably due to the small thickness of the  $\beta$ - $\text{Cu}_2\text{V}_2\text{O}_7$  coating made it difficult to detect  $\beta$ - $\text{Cu}_2\text{V}_2\text{O}_7$  by X-ray diffraction and, therefore, the presence of the reflection at  $2\theta = 24.7^\circ$ , in the case of the r-GO/ $\beta$ - $\text{Cu}_2\text{V}_2\text{O}_7/\text{TiO}_2$  has to be related to r-GO.

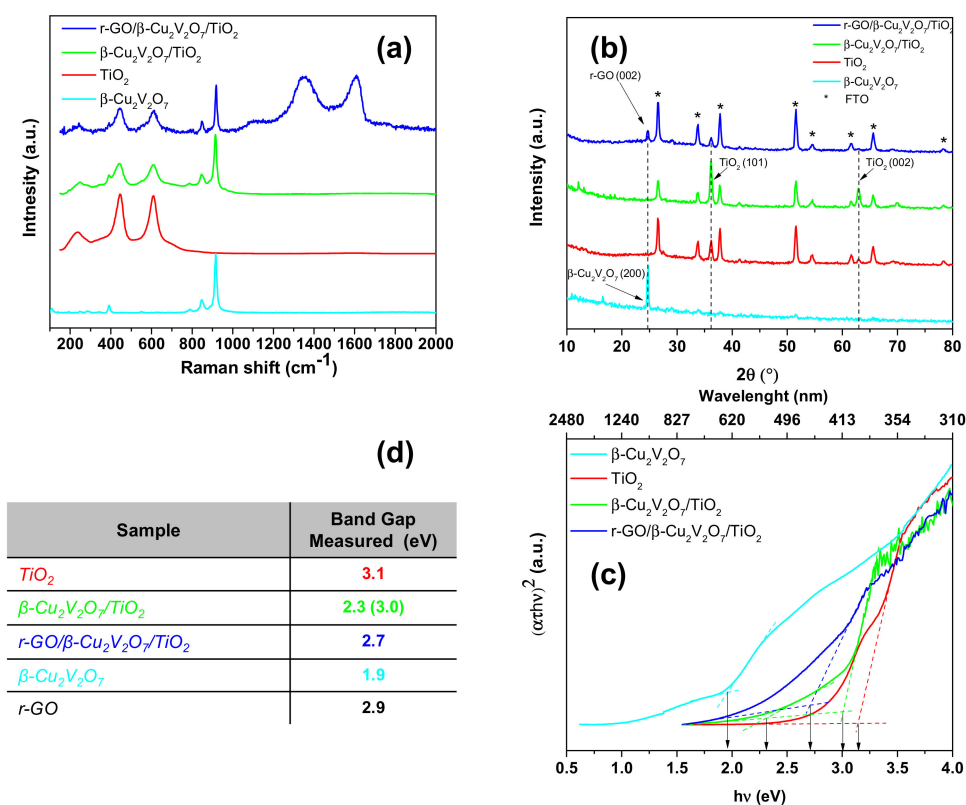


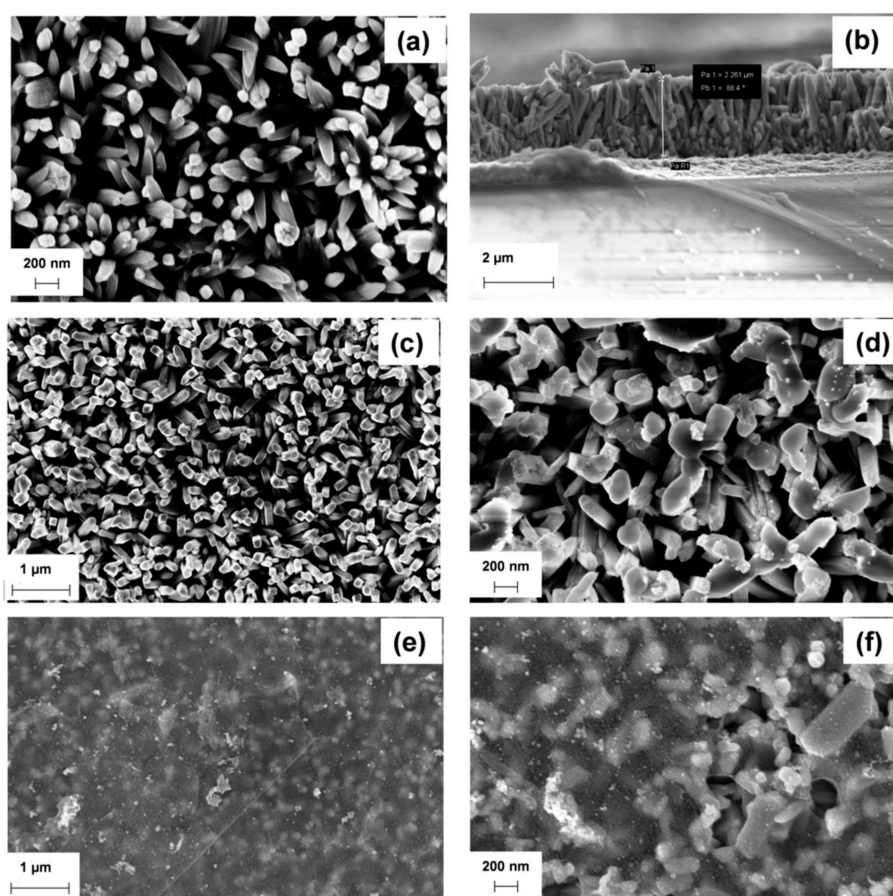
**Figure 1.** Raman spectra (a); wide angle X-ray diffraction (WAXD) patterns (b); and Tauc plots (c) of  $\beta$ -Cu<sub>2</sub>V<sub>2</sub>O<sub>7</sub>, TiO<sub>2</sub> NRs,  $\beta$ -Cu<sub>2</sub>V<sub>2</sub>O<sub>7</sub>/TiO<sub>2</sub> and GO/ $\beta$ -Cu<sub>2</sub>V<sub>2</sub>O<sub>7</sub>/TiO<sub>2</sub>; Bandgap values obtained from Tauc plots are indicated in the table on the left (d).

The band gap values ( $E_g$ ) of these semiconducting materials can be estimated from the Tauc plots (Figure 1c). The absorption coefficient is calculated from Equation (1):

$$C\alpha\tau = -\ln\left(\frac{T}{1-R_{\text{ref}}}\right) \quad (1)$$

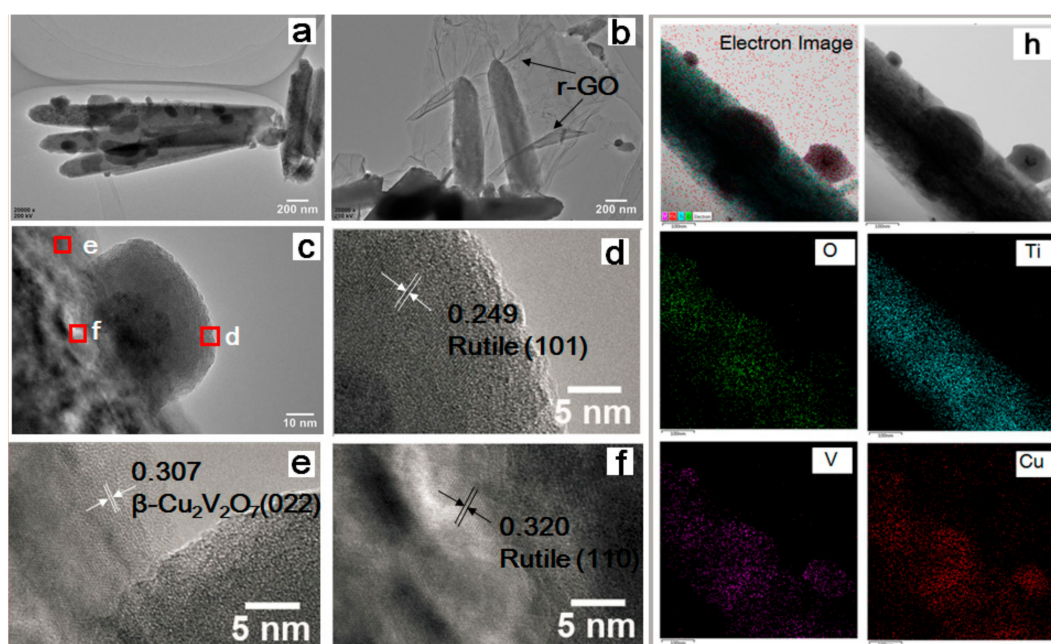
where  $\alpha$  is the absorption coefficient,  $\tau$  is the thickness of the film,  $C$  is a constant,  $T$  the transmittance, and  $R_{\text{ref}}$  the reflectance. Since all the samples studied were rather opaque it was necessary to acquire both the diffuse reflectance spectra and the transmittance spectra. The band gap ( $E_g$ ) was estimated by calculating the intercept of an extrapolated linear fit of the experimental data,  $[\alpha\tau hv]^2$ , to the flat portion of the plot, where no absorption occurs. The measured values of  $E_g$  for a direct transition are shown in Figure 1d [28].  $\beta$ -Cu<sub>2</sub>V<sub>2</sub>O<sub>7</sub> and TiO<sub>2</sub> show  $E_g$  values of 1.9 and 3.1 eV, respectively. Samples  $\beta$ -Cu<sub>2</sub>V<sub>2</sub>O<sub>7</sub>/TiO<sub>2</sub> and r-GO/ $\beta$ -Cu<sub>2</sub>V<sub>2</sub>O<sub>7</sub>/TiO<sub>2</sub> present a Tauc plot characterized by a shape typical of composite materials [11] with intercepts at ca. 3 eV ( $\beta$ -Cu<sub>2</sub>V<sub>2</sub>O<sub>7</sub>/TiO<sub>2</sub> presents an additional band gap at 2.3 eV related to copper vanadate particles) and 2.7 eV, after addition of r-GO (blue curve).

Figure 2 shows the SEM images of the pure TiO<sub>2</sub> NRs supported on FTO (Figure 2a) and those decorated with  $\beta$ -Cu<sub>2</sub>V<sub>2</sub>O<sub>7</sub> (Figure 2c,d) and coated with r-GO flakes (Figure 2e,f). The as annealed film consists of TiO<sub>2</sub> NRs with a diameter of ~50 nm and a length of ~2  $\mu$ m (Figure 2b). The sectional view, reported in Figure 2b, shows that these TiO<sub>2</sub> NRs are vertically aligned on the FTO substrate with a thickness of about 2–2.4  $\mu$ m. After the deposition of  $\beta$ -Cu<sub>2</sub>V<sub>2</sub>O<sub>7</sub>, the oxide nanoparticles stick randomly on the top of TiO<sub>2</sub> NRs surface (Figure 2c,d). Finally, the r-GO flakes tile the nanorods, similar to a silk coat. (Figure 2e,f).



**Figure 2.** Scanning electron microscope (SEM) images of: TiO<sub>2</sub> nanorods (NRs) on fluorine doped tin oxide (FTO) (a); cross-section of TiO<sub>2</sub> NRs (b); β-Cu<sub>2</sub>V<sub>2</sub>O<sub>7</sub>/TiO<sub>2</sub> (c,d); r-GO/β-Cu<sub>2</sub>V<sub>2</sub>O<sub>7</sub>/TiO<sub>2</sub> (e,f).

The TEM images and the corresponding energy dispersive X-ray (EDX) images are also presented in Figure 3. The size of the β-Cu<sub>2</sub>V<sub>2</sub>O<sub>7</sub> NPs is between 100 and 200 nm with a regular cubic shape (Figure 3a–c). According to the measurement of the lattice fringes ( $d = 0.249, 0.320,$  and  $0.307$  nm) there is a very good match with the crystallographic planes of rutile (101), rutile (110) and β-Cu<sub>2</sub>V<sub>2</sub>O<sub>7</sub> (022), respectively (Figure 3d–f). The O, Ti, V and Cu EDX elemental maps are also reported in Figure 3h together with the physical images. These images show that V and Cu are not only present on the vanadate NPs, but also on the surface of the NRs. The AASP deposition procedure allows the deposition of β-Cu<sub>2</sub>V<sub>2</sub>O<sub>7</sub> crystals not only on top of the rods, but also along their length, with variable dimensions caused by the diffusion of aerosol droplets through the porous TiO<sub>2</sub> NRs layer.



**Figure 3.** Transmission Electron Microscopy (TEM) images of  $\beta\text{-Cu}_2\text{V}_2\text{O}_7/\text{TiO}_2$  (a); and r-GO/ $\beta\text{-Cu}_2\text{V}_2\text{O}_7/\text{TiO}_2$  (b); High Resolution Transmission Electron Microscopy (HR-TEM) images of GO/ $\beta\text{-Cu}_2\text{V}_2\text{O}_7/\text{TiO}_2$  (c–f); morphology and energy dispersive X-ray (EDX) elemental mapping of r-GO/ $\beta\text{-Cu}_2\text{V}_2\text{O}_7/\text{TiO}_2$  NRs sample (h).

To obtain further information on the surface composition of these nanostructures the samples were characterized by XPS, before PEC measurements, as reported in Figure 4. Figure 4 shows the O 1s, V 2p<sub>3/2</sub> and Cu 2p<sub>3/2</sub> XPS spectra obtained from  $\beta\text{-Cu}_2\text{V}_2\text{O}_7/\text{TiO}_2$  (Figure 4a–c) and r-GO/ $\beta\text{-Cu}_2\text{V}_2\text{O}_7/\text{TiO}_2$  (Figure 4d–f). The O 1s XPS spectrum of  $\beta\text{-Cu}_2\text{V}_2\text{O}_7/\text{TiO}_2$  (Figure 4a) can be fitted with two components, located at about 529.8 and 532.0 eV, corresponding to lattice O<sup>2−</sup> ions from metal oxides and hydroxyl groups. In the case of the sample decorated with r-GO, the O 1s signal is mainly due to the oxygen atoms bound to carbon (Figure 4f) and can be fitted with three components at 531.0, 533.0 and 534.5 eV. These three components are due to (O=C) groups, alcoholic groups (HO–C) and water, respectively. The signal at about 529.9 eV, assigned to TiO<sub>2</sub> and vanadate lattice oxygens, is highly attenuated by the GO layers that coat the TiO<sub>2</sub> NRs (see SEM images) [29]. In the case of copper vanadate supported on TiO<sub>2</sub> NRs, without r-GO, the V 2p<sub>3/2</sub> signal (Figure 4b) can be fitted with only one component at 516.8 eV with a full width at half maximum (FWHM) of about 1.5 eV, corresponding to V<sup>5+</sup>, while in the case of the sample decorated with r-GO, Figure 4e, the signal contains two components at 516.4 and 517.5 eV corresponding to V<sup>4+</sup> and V<sup>5+</sup>, respectively [6]. It is interesting to note that the Cu 2p<sub>3/2</sub> signal (Figure 4c,d) indicates the presence of Cu<sup>2+</sup>, assigned to the component at 535.4 eV, and Cu<sup>+</sup> at 533.0 eV [30]. The Cu<sup>+</sup> signal, in the case of the sample treated with r-GO, is actually the main component (Cu<sup>2+</sup> 41% and Cu<sup>+</sup> 59%), indicating that some reaction has occurred between  $\beta\text{-Cu}_2\text{V}_2\text{O}_7$  and GO. This is confirmed also by the presence of a quite high amount of V<sup>4+</sup> (V<sup>5+</sup> is 62% and V<sup>4+</sup> is 38%) signal, while the Cu<sup>2+</sup>/V<sup>5+</sup> ratio (58% Cu<sup>2+</sup> and 42% V<sup>5+</sup>) is not too far from the 1:1 expected value for  $\beta\text{-Cu}_2\text{V}_2\text{O}_7$ . In the case of the  $\beta\text{-Cu}_2\text{V}_2\text{O}_7/\text{TiO}_2$  sample, the obtained Cu<sup>2+</sup>/V<sup>5+</sup> ratio is also close to the expected value (40% of Cu and 60% of V) and the presence of Cu<sup>+</sup> (Cu<sup>+</sup> 35.5%, Cu<sup>2+</sup> 64.5%) can be due to a photoreduction effect due to the X-ray source or to the presence of traces of CuO<sub>x</sub> [6].

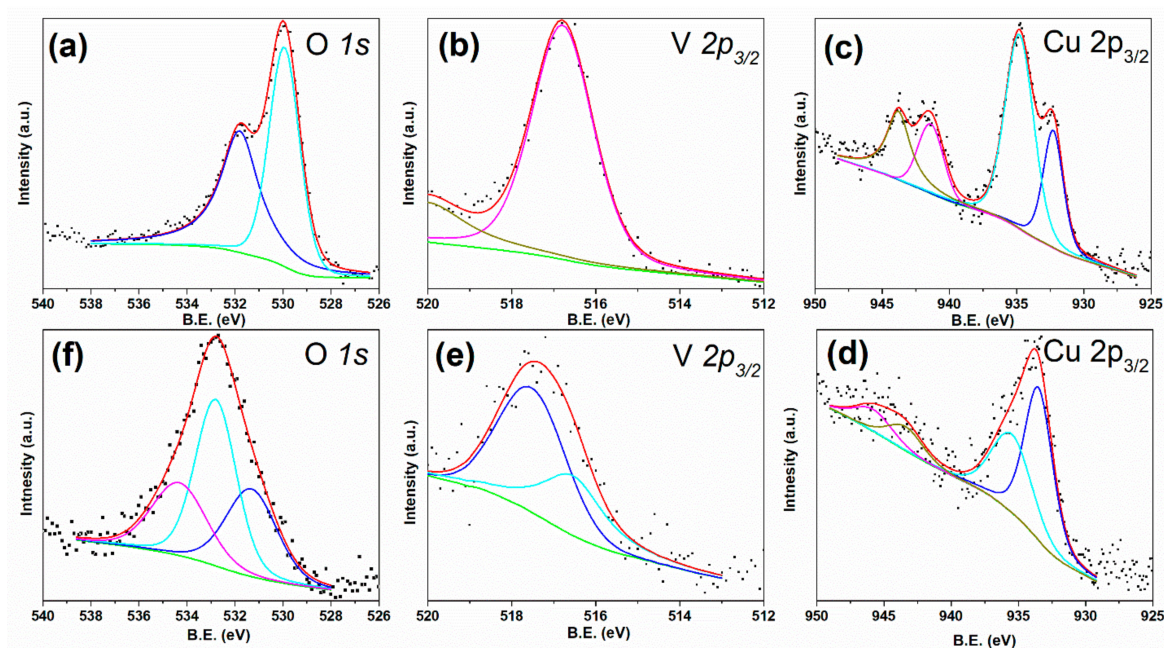


**Figure 4.** Spectroscopy (XPS) spectra of as-prepared  $\beta\text{-Cu}_2\text{V}_2\text{O}_7/\text{TiO}_2$  (a–c); and r-GO/ $\beta\text{-Cu}_2\text{V}_2\text{O}_7/\text{TiO}_2$  (d–f) samples.

All substrates were tested in PEC experiments, where the light source was a neutral white led with intensity ca.  $100 \text{ mW}/\text{cm}^2$  (Figure S4) in Na-borate buffer electrolyte (pH = 9.2). In Figure 5a, we report the linear voltammetry scans under chopped light for pure  $\beta\text{-Cu}_2\text{V}_2\text{O}_7$  deposits obtained using different ligands. From the plot it is easy to see that  $\text{NH}_3$  furnishes the better results in terms of photocurrent (ca.  $220 \mu\text{A}/\text{cm}^2$  at 1.55 V vs. RHE). For this reason, the decoration of  $\text{TiO}_2$  NRs by  $\beta\text{-Cu}_2\text{V}_2\text{O}_7$  was obtained by using  $\text{NH}_3$  in the precursor solution. As clearly visible in Figure 5b,c, the  $\text{TiO}_2$  NRs decorated with  $\beta\text{-Cu}_2\text{V}_2\text{O}_7$  show a better performance in terms of durability with almost no variation in the photocurrent after 3 h of EC work. On the contrary, the photocurrent density is lower with respect to the pure,  $\beta\text{-Cu}_2\text{V}_2\text{O}_7$  on FTO (Figure 5a).

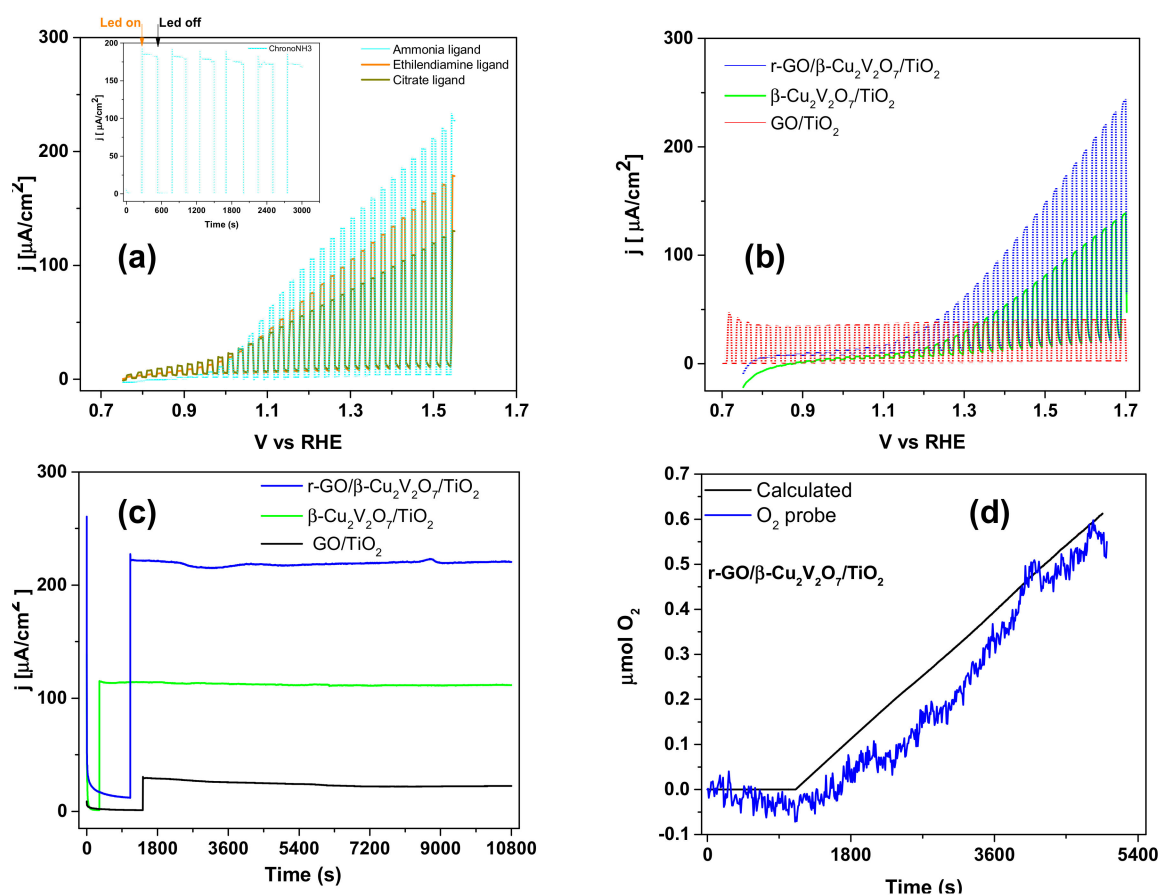


**Figure 5.** Photoelectrochemical performances: chopped Linear Sweep Voltammetry (LSV) (Borate Buffer pH = 9.2, scan rate 5 mV/s) of  $\beta\text{-Cu}_2\text{V}_2\text{O}_7$  deposited from aerosol solutions containing  $\text{NH}_3$ , EN or CA, as ligands, on FTO (a) (the inset shows a chronoamperometry at 1.5 V vs. Reversible Hydrogen Electrode (RHE) of a sample deposited with ammonia as ligand); chopped LSV (Borate Buffer pH = 9.2, scan rate 5 mV/s) of samples deposited on TiO<sub>2</sub> NRs (b); chronoamperometry of  $\beta\text{-Cu}_2\text{V}_2\text{O}_7/\text{TiO}_2$ , r-GO/ $\beta\text{-Cu}_2\text{V}_2\text{O}_7/\text{TiO}_2$  and r-GO/TiO<sub>2</sub> at 1.5 V vs. RHE (c); comparison of calculated and measured O<sub>2</sub> when r-GO/ $\beta\text{-Cu}_2\text{V}_2\text{O}_7/\text{TiO}_2$  is used as working electrode with light is set on at ca. 1000 s (d).

Addition of GO flakes by electrophoretic deposition allowed to obtain a much higher photocurrent density (see Figure 5b,c) and a very good durability. Finally, in Figure 5d, we report a comparison between the O<sub>2</sub> measured for the r-GO/ $\beta\text{-Cu}_2\text{V}_2\text{O}_7/\text{TiO}_2$  sample in the gas phase (head-space in a sealed electrochemical cell previously purged with N<sub>2</sub>), by an O<sub>2</sub> probe, based on the quenching of fluorescence, and the theoretical one, calculated from the recorded photocurrent. This measurement clearly demonstrates that the recorded photocurrent is not due to side processes like r-GO oxidation. The samples were also characterized by impedance spectroscopy (EIS) in the dark and under illumination at 1.5 V vs. RHE. From the data reported in Figure 6a,b it is evident that the samples  $\beta\text{-Cu}_2\text{V}_2\text{O}_7/\text{TiO}_2$  and, especially r-GO/ $\beta\text{-Cu}_2\text{V}_2\text{O}_7/\text{TiO}_2$ , are characterized by a much lower charge transfer resistance. The equivalent circuit used to fit the data [31] contains 2 RQ elements (parallel connection of an ohmic resistance R and a constant phase element Q), in the case of pure  $\beta\text{-Cu}_2\text{V}_2\text{O}_7$  on FTO, while for the composite materials  $\beta\text{-Cu}_2\text{V}_2\text{O}_7/\text{TiO}_2$  and r-GO/ $\beta\text{-Cu}_2\text{V}_2\text{O}_7/\text{TiO}_2$ , we have used a series of 3 RQ elements. This circuit is represented in Figure 6d where the R<sub>s</sub> represents the solution resistance, the first RQ element the double layer, the second one the Cu-vanadate layer and the third one the TiO<sub>2</sub> NRs. It is interesting to point out that upon illumination only the second circuit (R<sub>2</sub>) shows a very strong decrease in the charge transfer resistance, while the other 2 circuits present

only minor variations. This is a strong indication that it is mainly the Cu-vanadate layer that acts as the active material in the water photo-oxidation, while the role of  $\text{TiO}_2$  is simply that of a substrate.

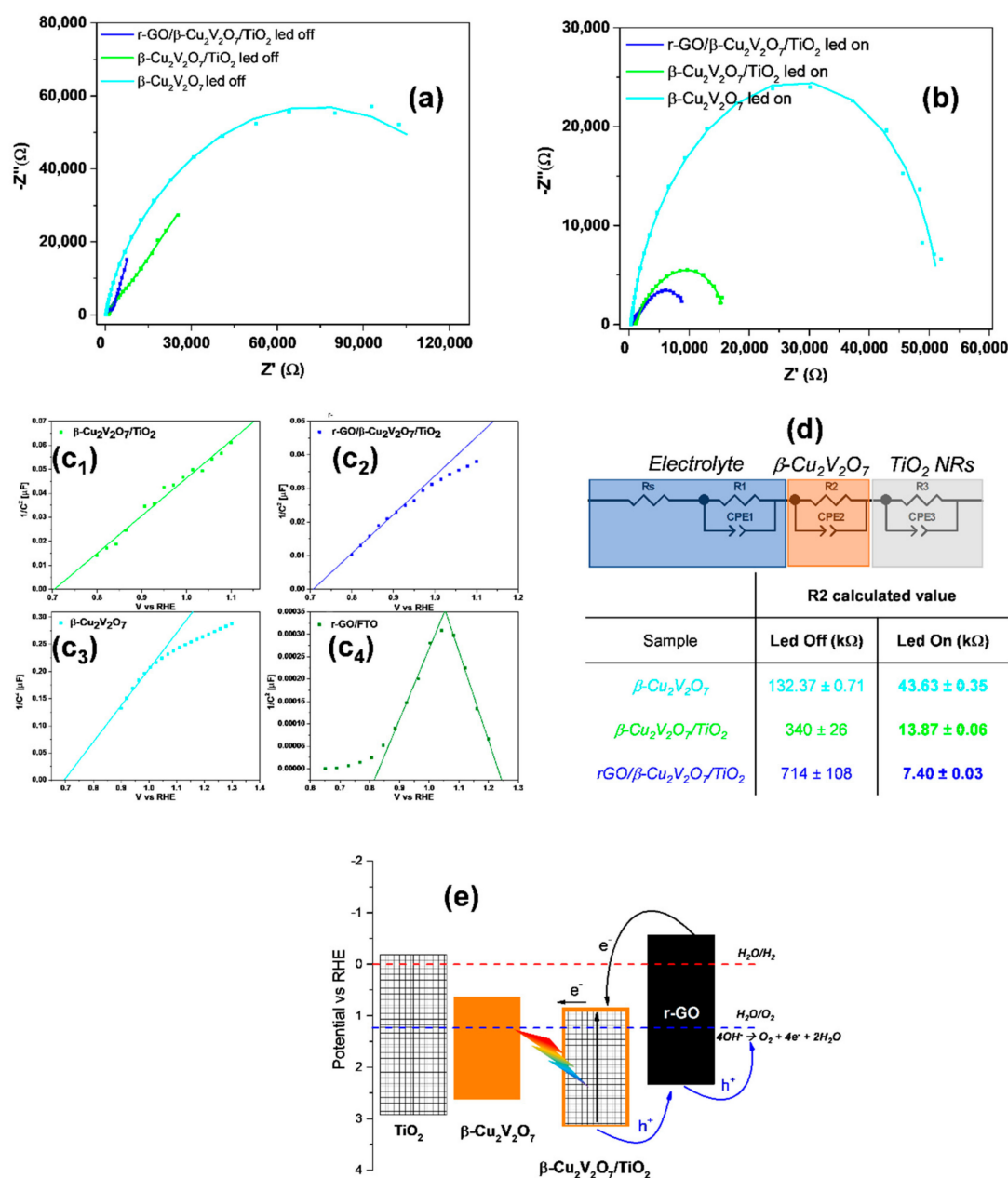


**Figure 6.** Nyquist plots obtained with samples polarized at 1.5 V vs RHE in the dark (a); and under illumination (b); Mott-Schottky plots for  $\beta\text{-Cu}_2\text{V}_2\text{O}_7/\text{TiO}_2$  (c<sub>1</sub>), r-GO/ $\beta\text{-Cu}_2\text{V}_2\text{O}_7/\text{TiO}_2$  (c<sub>2</sub>),  $\beta\text{-Cu}_2\text{V}_2\text{O}_7$  (c<sub>3</sub>), r-GO/FTO (c<sub>4</sub>); EIS equivalent circuit [31] (d); schematic representation of band edges approximate position for r-GO/ $\beta\text{-Cu}_2\text{V}_2\text{O}_7/\text{TiO}_2$  sample (e) Band edges positions for  $\beta\text{-Cu}_2\text{V}_2\text{O}_7$  and  $\text{TiO}_2$  are added for comparison.

In Figure 6c we report also the Mott-Schottky (MS) plots (in the range 1–10<sup>5</sup> Hz) obtained from pure  $\beta\text{-Cu}_2\text{V}_2\text{O}_7$ ,  $\beta\text{-Cu}_2\text{V}_2\text{O}_7/\text{TiO}_2$  and r-GO/ $\beta\text{-Cu}_2\text{V}_2\text{O}_7/\text{TiO}_2$ . The relation between the flat-band potential ( $V_{fb}$ ) and the material capacity ( $C$ ) is reported in Equation (2).  $N_{SC}$  indicates the carrier's concentration in the space charge of the material,  $\epsilon$  the dielectric constant,  $e$  is the electron charge and

$A$  is the area of the electrode. n-types semiconductors, like  $\text{TiO}_2$  and  $\beta\text{-Cu}_2\text{V}_2\text{O}_7$ , are characterized by positive slopes, while p-types materials have negative slopes.

$$\frac{1}{C^2} = \frac{2(V - V_{fb})}{eN_{sc}\epsilon A^2} \quad (2)$$

The capacity values were calculated by fitting the impedance data with a Randle's circuit containing Constant Phase Elements (CPE) instead of ideal capacitors. Thus, the capacity was calculated from Brugg's Equation (3) [32]

$$C = (Q)^{\frac{1}{p}} \left( R_s^{-1} + R_p^{-1} \right)^{\left(1 - \frac{1}{p}\right)} \quad (3)$$

where  $Q$  and  $p$ , are fitting parameters from CPE elements,  $R_s$  is the cell resistance and  $R_p$  is the resistance in parallel with CPE elements. By plotting  $C^{-2}$  vs. RHE it is possible to determine  $V_{fb}$  and from this value to derive the approximate position of conduction (CB) and valence (VB) edges. The relation between  $V_{fb}$  and bands edges ( $E_{cb}$  and  $E_{vb}$ ) can be expressed by Equations (4) and (5) [33]:

$$E_{cb} = V_{fb} + k_b T \ln \left( \frac{N_{sc}}{N_{cb}} \right) \quad (4)$$

$$E_{vb} = -V_{fb} + k_b T \ln \left( \frac{N_{sc}}{N_{vb}} \right) \quad (5)$$

where  $N_{cb}$  and  $N_{vb}$ , are the effective density of states in the CB and VB for a n-type and p-type semiconductors, respectively. In the case of n-type conductivity Equation (4) is usually approximated with  $E_{cb} \approx V_{fb} + 0.1$  eV [8]. Thus, the MS plots reported in Figure 6c, show how the decoration of  $\text{TiO}_2$  does not change band edges position of the copper vanadate ( $\text{TiO}_2$  acts as a support), while the addition of p-type GO, probably produces many p-n nano-junctions with  $\beta\text{-Cu}_2\text{V}_2\text{O}_7/\text{TiO}_2$  (see scheme of Figure 6d, although not visible from the MS plot of Figure 6c<sub>2</sub>). Indeed, the lower slope of the MS plot of Figure 6c<sub>2</sub> indicates a higher concentration of electrons ( $1 \times 10^{17} \text{ m}^{-3}$  for  $\beta\text{-Cu}_2\text{V}_2\text{O}_7/\text{TiO}_2$  and  $1.4 \times 10^{17} \text{ m}^{-3}$  for the sample decorated with r-GO), as already seen in the case of  $\text{TiO}_2$  nanorods decorated with  $\text{Cu}_2\text{O}$  nanoparticles [34]. Finally, the p-type conductivity of r-GO is clearly seen from the MS plot obtained from a pure r-GO sample deposited on FTO and thermally treated at 200 °C for 15 min (Figure 6c<sub>4</sub>).

More precise details about the surface composition of these nanostructures can be obtained by acquiring XPS data after electrochemical work. The results of this analysis are summarized in Figure 7 and Table 1. Figure 7a,b shows the O 1s, V 2p and Cu 2p XPS spectra obtained from  $\beta\text{-Cu}_2\text{V}_2\text{O}_7/\text{TiO}_2$  NRs after 3 h of electrochemical measurements, under illumination. The O 1s XPS spectrum can be fitted with two components located at about 529.9 and 532.0 eV that correspond to lattice  $\text{O}^{2-}$  ions from  $\beta\text{-Cu}_2\text{V}_2\text{O}_7$  and  $\text{TiO}_2$  and hydroxyls groups [35]. The V 2p<sub>3/2</sub> signal (in Figure 7a), can be fitted with two components at 516.0, weak, and 517.0 eV corresponding to  $\text{V}^{4+}$  and  $\text{V}^{5+}$  respectively. The Cu 2p<sub>3/2</sub> signals (Figure 7b) contains two components, one at 935.0 and another at 933.0 eV indicating the presence of  $\text{Cu}^{2+}$  and a considerable quantity of  $\text{Cu}^+$ . The presence of  $\text{Cu}^+$  is probably caused by a photo-reduction effect and eventually by X-rays in UHV. In Figure 7c we show also the C 1s spectra acquired from a sample of r-GO/ $\beta\text{-Cu}_2\text{V}_2\text{O}_7/\text{TiO}_2$  after PEC work. The region can be fitted with 3 components at 284.1, 285.7 and 288.0 eV corresponding respectively to C–C, C–O and C=O bonds [26]. The relative intensity and positions of these signals are fully compatible with p-type r-GO oxide, after a mild heat treatment [36]. A simple visual inspection of the O 1s and V 2p region, reported in Figure 7d, reveals how the amount of V in the case of the r-GO/ $\beta\text{-Cu}_2\text{V}_2\text{O}_7/\text{TiO}_2$  is significantly lower if compared with the sample not containing GO. In fact, the V 2p signal is much lower with respect to the O 1s signal at 529.4 eV. Moreover, the Cu 2p signal, reported in Figure 7e, shows mostly the presence of  $\text{Cu}^+$  deduced from the position (933.0 eV) and the very low intensity of the satellites

peaks. This fact is in agreement with what already verified on the sample before PEC work where the high amount of  $\text{Cu}^+$  and the high Cu/V ratio indicated that the addition of GO modified the composition of the vanadate.

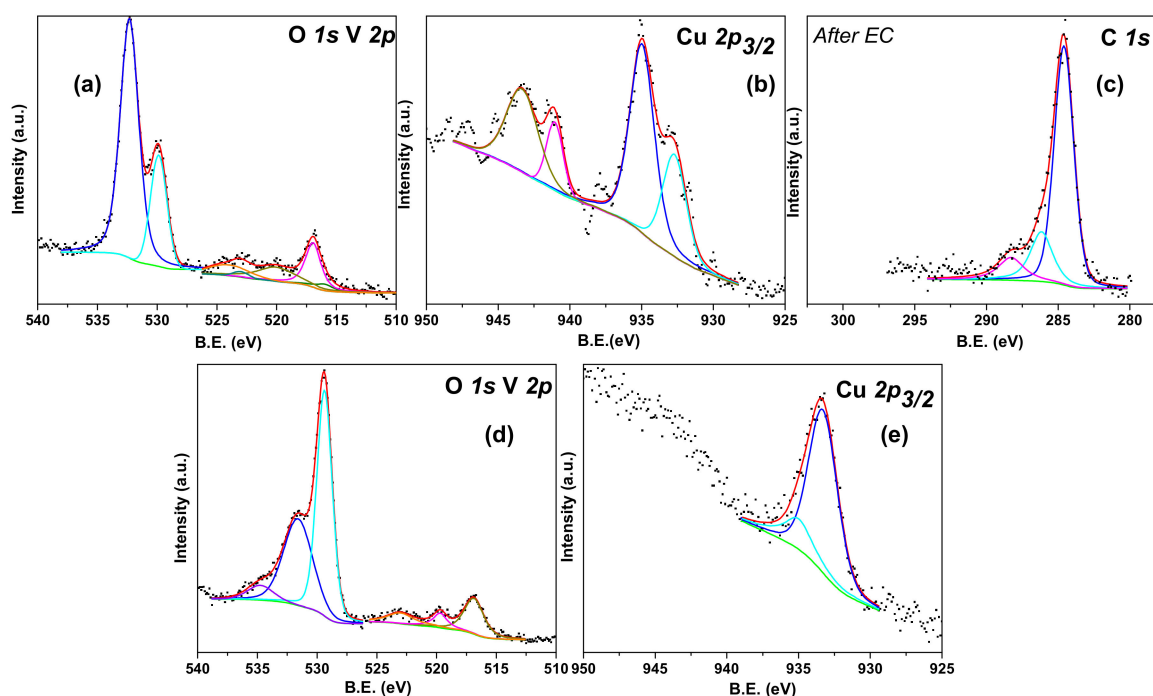


**Figure 7.** XPS spectra of samples  $\beta\text{-Cu}_2\text{V}_2\text{O}_7/\text{TiO}_2$  after Electrochemical work (a–b); and of r-GO/ $\beta\text{-Cu}_2\text{V}_2\text{O}_7/\text{TiO}_2$  after photoelectrochemical (PEC) work.

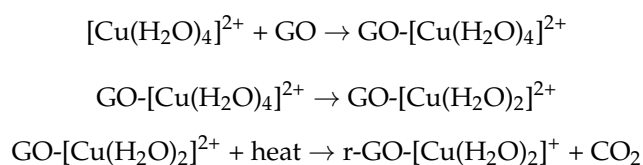
The Cu/V ratios obtained from XPS data after EC work are similar to those obtained before EC (Raman spectra and SEM images after EC are reported in Figures S6 and S7, respectively). In the case of  $\beta\text{-Cu}_2\text{V}_2\text{O}_7/\text{TiO}_2$  we found a 52% abundance of  $\text{V}^{5+}$  and 48% for  $\text{Cu}^{2+}$ , with a rather high amount of  $\text{Cu}^+$  (Figure 7b). In the case of the sample decorated with r-GO, the amount of  $\text{Cu}^{2+}$  is 32%, while the amount of  $\text{V}^{5+}$  is 68%. In this last case the large quantity of  $\text{Cu}^+$  seems to be due to the presence of the GO layer.

**Table 1.** Cu and V percent abundance from XPS data.

Element Abundance	Before PEC		After PEC	
	$\text{Cu}^{2+}$	$\text{V}^{5+}$	$\text{Cu}^{2+}$	$\text{V}^{5+}$
Sample				
r-GO/ $\beta\text{-Cu}_2\text{V}_2\text{O}_7/\text{TiO}_2$	58	42	32	68
$\beta\text{-Cu}_2\text{V}_2\text{O}_7/\text{TiO}_2$	40	60	52	48

All the above reported data indicate that supporting  $\beta\text{-Cu}_2\text{V}_2\text{O}_7$  on  $\text{TiO}_2$  NRs allows the obtainment of a material with good durability, as photoanode, with a much lower charge transfer resistance as testified by the EIS data (Figure 6a,b). The interaction between the  $\text{TiO}_2$  NRs and  $\beta\text{-Cu}_2\text{V}_2\text{O}_7$  has a favorable effect on the photocurrent production since the deposition of  $\text{V}_2\text{O}_5$  on  $\text{TiO}_2$  NRs, by the same AASP process, does not lead to any particular enhancement in the photocurrent if compared with untreated  $\text{TiO}_2$  (see Figures S8 and S9). It's also known that the decoration of Degussa P25 by  $\text{CuO}$  nanoparticles actually leads to a modest enhancement of photocurrent values [37]. A significant improvement in the photocurrent density can be achieved by decorating the  $\beta\text{-Cu}_2\text{V}_2\text{O}_7/\text{TiO}_2$  sample by GO followed by heat treatment at about 200 °C. The addition of GO changes the Cu/V ratio leading to high amount of  $\text{Cu}^+$  as testified by the XPS spectra, acquired

before and after EC work. We think that the better performance in terms of photocurrent is due to the combination of r-GO/ $\beta$ -Cu<sub>2</sub>V<sub>2</sub>O<sub>7</sub>/TiO<sub>2</sub> since the addition of r-GO to TiO<sub>2</sub> NRs did not lead to any particular improvement in the photocurrent, as is clearly visible in Figure 5b. We verified that the interaction of GO with  $\beta$ -Cu<sub>2</sub>V<sub>2</sub>O<sub>7</sub> and heat treatment at 200 °C, after the electrophoretic deposition of GO, actually leads to the formation of p-type r-GO with a band gap, as measured from the UV–Vis spectra (see Figure S10) of about 2.5–2.7 eV. We can justify the interaction of GO with  $\beta$ -Cu<sub>2</sub>V<sub>2</sub>O<sub>7</sub>, that leads to the variation in the Cu/V ratio, as caused by the relatively low pH of the GO suspension (pH = 6.5), used during the electrophoretic deposition process, and by the GO itself. In fact, the solubility of  $\beta$ -Cu<sub>2</sub>V<sub>2</sub>O<sub>7</sub> increases at low pH and, at the same time, the GO sheets can easily co-ordinate the Cu<sup>2+</sup> ions [38]. The Cu<sup>2+</sup> ions, once chemisorbed on the GO nano-sheets, most probably by the carboxylic groups, can be reduced by GO and most probably by the heat treatment, with formation of CO<sub>2</sub> as summarized in the following reaction sequence [38]:



As known and reported in several publications, the mild thermal treatment at 200–210 °C that leads to the formation of a partially reduced GO has to be intended formally as a disproportionate reaction where the electrons released with O<sub>2</sub>, CO or CO<sub>2</sub> evolution are used to reduce the GO surface [39,40]. In this particular case, we think that this process leads also to the formation of Cu<sup>+</sup> species as Cu<sub>2</sub>O nanoparticles. Since the  $V_{fb}$  is the same for  $\beta$ -Cu<sub>2</sub>V<sub>2</sub>O<sub>7</sub>,  $\beta$ -Cu<sub>2</sub>V<sub>2</sub>O<sub>7</sub>/TiO<sub>2</sub> and r-GO/ $\beta$ -Cu<sub>2</sub>V<sub>2</sub>O<sub>7</sub>/TiO<sub>2</sub> and the Cu<sup>2+</sup>/V<sup>5+</sup> ratio on r-GO/ $\beta$ -Cu<sub>2</sub>V<sub>2</sub>O<sub>7</sub>/TiO<sub>2</sub> is compatible with a 1:2 value, we can formulate the hypothesis that the vanadate partially decomposes forming Cu<sub>2</sub>O nanoparticles on the GO flakes and on the NRs surface, while remaining still on the TiO<sub>2</sub> surface, in lower amounts, in a form compatible with the a “CuV<sub>2</sub>O<sub>6</sub>” stoichiometry. The position of band edges of r-GO with respect to the band edges of the composite material,  $\beta$ -Cu<sub>2</sub>V<sub>2</sub>O<sub>7</sub>/TiO<sub>2</sub>, is particularly favorable to form many p-n nano-junctions, as depicted in Figure 6d, leading to a better charge separation, increase in the photocurrent density and improved durability. It is important to note that the slightly higher position of  $E_{cb}$  of pure TiO<sub>2</sub> NRs (slightly above the H<sup>+</sup>/H<sub>2</sub> reduction potential) would have led to a less favorable junction with p-type r-GO. Finally, the possible formation of a further p-n junction between the Cu<sub>2</sub>O nanoparticle and the TiO<sub>2</sub> surface should also be taken into account [34].

#### 4. Conclusions

We have prepared  $\beta$ -Cu<sub>2</sub>V<sub>2</sub>O<sub>7</sub>/TiO<sub>2</sub> and r-GO/ $\beta$ -Cu<sub>2</sub>V<sub>2</sub>O<sub>7</sub>/TiO<sub>2</sub> composite materials with the aim of obtaining visible light driven photoanodes. The vanadate deposition was obtained by an easy & fast aerosol assisted spray pyrolysis procedure. The  $\beta$ -Cu<sub>2</sub>V<sub>2</sub>O<sub>7</sub>/TiO<sub>2</sub> composite material showed a better durability if compared with pure  $\beta$ -Cu<sub>2</sub>V<sub>2</sub>O<sub>7</sub> deposited on FTO and a lower charge transfer resistance as indicated by EIS data. The addition of p-type r-GO to  $\beta$ -Cu<sub>2</sub>V<sub>2</sub>O<sub>7</sub>/TiO<sub>2</sub> had a positive effect on durability, charge transfer resistance and photocurrent density. As verified by XPS analysis, the GO addition, by electrophoretic deposition, led to a strong interaction with  $\beta$ -Cu<sub>2</sub>V<sub>2</sub>O<sub>7</sub> with formation of r-GO flakes and Cu<sub>2</sub>O nanoparticles. The amount of O<sub>2</sub> produced, upon visible light illumination, independently measured by an O<sub>2</sub> probe, indicated that this composite material is characterized by a good faradaic efficiency. The easy and fast procedure that allows its preparation can be easily extended, with low cost, to electrodes with a larger area.

**Supplementary Materials:** The following are available online at <http://www.mdpi.com/2079-4991/8/7/544/s1>. Figure S1. Chopped Linear Sweep Voltammetry of sample r-GO/ $\beta$ -Cu<sub>2</sub>V<sub>2</sub>O<sub>7</sub>/TiO<sub>2</sub> in Na sulfate electrolyte; Figure S2. Chronoamperometry from sample r-GO/ $\beta$ -Cu<sub>2</sub>V<sub>2</sub>O<sub>7</sub>/TiO<sub>2</sub> at 1.75 V vs. RHE; Figure S3. Drawing of the photoelectrochemical cell (Proteus Gamma I—PINE Research) (CE = Counter Electrode; RE = Reference

Electrode); Figure S4. Emission spectrum of white LED light used in all the reported PEC measurements; Figure S5. Chopped LSV on r-GO/ $\beta$ -Cu<sub>2</sub>V<sub>2</sub>O<sub>7</sub>/TiO<sub>2</sub> sample with front and back illumination (ca. 100 mW/cm<sup>2</sup>) in borate buffer solution; Figure S6. (a) Raman spectra before and after PEC work obtained from different areas of sample r-GO/ $\beta$ -Cu<sub>2</sub>V<sub>2</sub>O<sub>7</sub> after (b) and before (c) PEC work; Figure S7. SEM image of sample r-GO/ $\beta$ -Cu<sub>2</sub>V<sub>2</sub>O<sub>7</sub>/TiO<sub>2</sub> after PEC work; Figure S8. Chopped Linear Sweep Voltammetry of the TiO<sub>2</sub> nanorods substrate in borate buffer (pH = 9.2) with led light intensity of ca. 100 mW/cm<sup>2</sup>; Figure S9. Chopped Linear Sweep Voltammetry of TiO<sub>2</sub> NRs decorated with V<sub>2</sub>O<sub>5</sub> nanoparticles in borate buffer (pH = 9.2); Figure S10. Tauc Plot of r-GO deposited by electrophoresis on FTO slides.

**Author Contributions:** G.A.R. conceived and designed the experiments; L.G., S.S., C.M. and A.S. performed the experiments; Z.Z. and G.A.R. analyzed the data; G.G. and G.A.R. wrote the paper. We would like to thank Luca Bardini for helpful discussions.

**Acknowledgments:** Authors gratefully acknowledge the Italian Minister of University (MIUR) for financial support to the SMARTNESS (Solar driven chemistry: new materials for photo- and electrocatalysis) financed thorough the PRIN 2015K7FZLH. Thanks are due to the MAECI (Ministero degli Affari Esteri e della Cooperazione Internazionale) for the support through the bilateral Italy–China GRAPE-MAT project. SS thanks the China Scholarship Council (CSC) for a grant to spend one year at University of Padova.

**Conflicts of Interest:** The authors declare no conflict of interest.

## References

1. Muradov, N.Z.; Veziroğlu, T.N. From hydrocarbon to hydrogen-carbon to hydrogen economy. *Int. J. Hydrogen Energy* **2005**, *30*, 225–237. [[CrossRef](#)]
2. Walter, M.G.; Warren, E.L.; McKone, J.R.; Boettcher, S.W.; Mi, Q.; Santori, E.A.; Lewis, N.S. Solar water splitting cells. *Chem. Rev.* **2010**, *110*, 6446–6473. [[CrossRef](#)] [[PubMed](#)]
3. Osterloh, F.E. Inorganic Materials as Catalysts for Photoelectrochemical Splitting of Water. *Chem. Mater.* **2008**, *20*, 35. [[CrossRef](#)]
4. Newhouse, P.F.; Boyd, D.A.; Shinde, A.; Guevarra, D.; Zhou, L.; Soedarmadji, E.; Li, G.; Neaton, J.B.; Gregoire, J.M. Solar fuel photoanodes prepared by inkjet printing of copper vanadates. *J. Mater. Chem. A* **2016**, *4*, 7483–7494. [[CrossRef](#)]
5. Fountaine, K.T.; Lewerenz, H.J.; Atwater, H.A. Efficiency limits for photoelectrochemical water-splitting. *Nat. Commun.* **2016**, *7*, 1–9. [[CrossRef](#)] [[PubMed](#)]
6. Zhou, L.; Yan, Q.; Yu, J.; Jones, R.J.R.; Becerra-Stasiewicz, N.; Suram, S.K.; Shinde, A.; Guevarra, D.; Neaton, J.B.; Persson, K.A.; et al. Stability and self-passivation of copper vanadate photoanodes under chemical, electrochemical, and photoelectrochemical operation. *Phys. Chem. Chem. Phys.* **2016**, *18*, 9349–9352. [[CrossRef](#)] [[PubMed](#)]
7. Seabold, J.A.; Neale, N.R. All first row transition metal oxide photoanode for water splitting based on Cu<sub>3</sub>V<sub>2</sub>O<sub>8</sub>. *Chem. Mater.* **2015**, *27*, 1005–1013. [[CrossRef](#)]
8. Guo, W.; Chemelewski, W.D.; Mabayoje, O.; Xiao, P.; Zhang, Y.; Mullins, C.B. Synthesis and Characterization of CuV<sub>2</sub>O<sub>6</sub> and Cu<sub>2</sub>V<sub>2</sub>O<sub>7</sub>: Two Photoanode Candidates for Photoelectrochemical Water Oxidation. *J. Phys. Chem. C* **2015**, *119*, 27220–27227. [[CrossRef](#)]
9. Jiang, C.M.; Segev, G.; Hess, L.H.; Liu, G.; Zaborski, G.; Toma, F.M.; Cooper, J.K.; Sharp, I.D. Composition-Dependent Functionality of Copper Vanadate Photoanodes. *ACS Appl. Mater. Interfaces* **2018**, *10*, 10627–10633. [[CrossRef](#)]
10. Liu, B.; Aydil, E.S. Growth of oriented single-crystalline rutile TiO<sub>2</sub> nanorods on transparent conducting substrates for dye-sensitized solar cells. *J. Am. Chem. Soc.* **2009**, *131*, 3985–3990. [[CrossRef](#)] [[PubMed](#)]
11. Sun, J.; Li, X.; Zhao, Q.; Ke, J.; Zhang, D. Novel V<sub>2</sub>O<sub>5</sub>/BiVO<sub>4</sub>/TiO<sub>2</sub> nanocomposites with high visible-light-induced photocatalytic activity for the degradation of toluene. *J. Phys. Chem. C* **2014**, *118*, 10113–10121. [[CrossRef](#)]
12. Hu, Y.; Li, D.; Zheng, Y.; Chen, W.; He, Y.; Shao, Y.; Fu, X.; Xiao, G. BiVO<sub>4</sub>/TiO<sub>2</sub> nanocrystalline heterostructure: A wide spectrum responsive photocatalyst towards the highly efficient decomposition of gaseous benzene. *Appl. Catal. B Environ.* **2011**, *104*, 30–36. [[CrossRef](#)]
13. Wang, C.; Chen, Z.; Jin, H.; Cao, C.; Li, J.; Mi, Z. Enhancing visible-light photoelectrochemical water splitting through transition-metal doped TiO<sub>2</sub> nanorod arrays. *J. Mater. Chem. A* **2014**, *2*, 17820–17827. [[CrossRef](#)]

14. Chen, X. Juan; Dai, Y. zhi; Wang, X. yan; Guo, J.; Liu, T. hua; Li, F.F. Synthesis and characterization of Ag<sub>3</sub>PO<sub>4</sub> immobilized with graphene oxide (GO) for enhanced photocatalytic activity and stability over 2,4-dichlorophenol under visible light irradiation. *J. Hazard. Mater.* **2015**, *292*, 9–18. [[CrossRef](#)] [[PubMed](#)]
15. Bai, Y.-Y.; Wang, F.-R.; Liu, J.-K. A New Complementary Catalyst and Catalytic Mechanism: Ag<sub>2</sub>MoO<sub>4</sub>/Ag/AgBr/GO Heterostructure. *Ind. Eng. Chem. Res.* **2016**, *55*, 9873–9879. [[CrossRef](#)]
16. Thomas, A.V.; Andow, B.C.; Suresh, S.; Eksik, O.; Yin, J.; Dyson, A.H.; Koratkar, N. Controlled crumpling of graphene oxide films for tunable optical transmittance. *Adv. Mater.* **2015**, *27*, 3256–3265. [[CrossRef](#)] [[PubMed](#)]
17. Mohd Zaid, H.F.; Chong, F.K.; Abdul Mutalib, M.I. Photooxidative-extractive deep desulfurization of diesel using Cu-Fe/TiO<sub>2</sub> and eutectic ionic liquid. *Fuel* **2015**, *156*, 54–62. [[CrossRef](#)]
18. Lü, X.; Yang, W.; Quan, Z.; Lin, T.; Bai, L.; Wang, L.; Huang, F.; Zhao, Y. Enhanced Electron Transport in Nb-Doped TiO<sub>2</sub> Nanoparticles via Pressure-Induced Phase Transitions. *J. Am. Chem. Soc.* **2014**, *136*, 419–426. [[CrossRef](#)] [[PubMed](#)]
19. Williams, G.; Seger, B.; Kamat, P. TiO<sub>2</sub>-Graphene Nanocomposites. UV-Assisted Photocatalytic Reduction of Graphene Oxide. *ACS Nano* **2008**, *2*, 1487–1491.
20. Yeh, T.F.; Cihlář, J.; Chang, C.Y.; Cheng, C.; Teng, H. Roles of graphene oxide in photocatalytic water splitting. *Mater. Today* **2013**, *16*, 78–84. [[CrossRef](#)]
21. White, R.; Thomas, P.S.; Philips, M.R.; Wuhrer, R.; Guerbois, J.P. TG-MS characterization of the reaction products of cadmium yellow and malachite artist's pigments. *J. Therm. Anal. Calorim.* **2007**, *88*, 181–184. [[CrossRef](#)]
22. Wang, J.; Qu, S.; Zhong, Z.; Wang, S.; Liu, K.; Hu, A. Fabrication of TiO<sub>2</sub> nanoparticles/nanorod composite arrays via a two-step method for efficient dye-sensitized solar cells. *Prog. Nat. Sci. Mater. Int.* **2014**, *24*, 588–592. [[CrossRef](#)]
23. Marcano, D.C.; Kosynkin, D.V.; Berlin, J.M.; Sinitskii, A.; Sun, Z.; Slesarev, A.; Alemany, L.B.; Lu, W.; Tour, J.M. Improved Synthesis of Graphene Oxide. *ACS Nano* **2010**, *4*. [[CrossRef](#)] [[PubMed](#)]
24. Frank, O.; Zukalova, M.; Laskova, B.; Kürti, J.; Koltai, J.; Kavan, L. Raman spectra of titanium dioxide (anatase, rutile) with identified oxygen isotopes (16, 17, 18). *Phys. Chem. Chem. Phys.* **2012**, *14*, 14567. [[CrossRef](#)] [[PubMed](#)]
25. De Waal, D.; Hutter, C. Vibrational spectra of two phases of copper pyrovanadate and some solid solutions of copper and magnesium pyrovanadate. *Mater. Res. Bull.* **1994**, *29*, 843–849. [[CrossRef](#)]
26. How, G.T.S.; Pandikumar, A.; Ming, H.N.; Ngee, L.H. Highly exposed {001} facets of titanium dioxide modified with reduced graphene oxide for dopamine sensing. *Sci. Rep.* **2014**, *4*, 2–9. [[CrossRef](#)] [[PubMed](#)]
27. Mishra, S.K.; Tripathi, S.N.; Choudhary, V.; Gupta, B.D. SPR based fibre optic ammonia gas sensor utilizing nanocomposite film of PMMA/reduced graphene oxide prepared by in situ polymerization. *Sens. Actuators B Chem.* **2014**, *199*, 190–200. [[CrossRef](#)]
28. Viezbicke, B.D.; Patel, S.; Davis, B.E.; Birnie, D.P. Evaluation of the Tauc method for optical absorption edge determination: ZnO thin films as a model system. *Phys. Status Solidi* **2015**, *252*, 1700–1710. [[CrossRef](#)]
29. Shuang, S.; Lv, R.; Xie, Z.; Wang, W.; Cui, X.; Ning, S.; Zhang, Z.  $\alpha$ -Fe<sub>2</sub>O<sub>3</sub> nanopillar arrays fabricated by electron beam evaporation for the photoassisted degradation of dyes with H<sub>2</sub>O<sub>2</sub>. *RSC Adv.* **2016**, *6*, 534–540. [[CrossRef](#)]
30. Li, H.; Su, Z.; Hu, S.; Yan, Y. Free-standing and flexible Cu/Cu<sub>2</sub>O/CuO heterojunction net: A novel material as cost-effective and easily recycled visible-light photocatalyst. *Appl. Catal. B Environ.* **2017**, *207*, 134–142. [[CrossRef](#)]
31. Hernández, S.; Hidalgo, D.; Sacco, A.; Chiodoni, A.; Lamberti, A.; Cauda, V.; Tresso, E.; Saracco, G. Comparison of photocatalytic and transport properties of TiO<sub>2</sub> and ZnO nanostructures for solar-driven water splitting. *Phys. Chem. Chem. Phys.* **2015**, *17*, 7775–7786. [[CrossRef](#)] [[PubMed](#)]
32. Kwolek, P.; Szaciłowski, K. Photoelectrochemistry of n-type bismuth oxyiodide. *Electrochim. Acta* **2013**, *104*, 448–453. [[CrossRef](#)]
33. Pastor-Moreno, G. Chapter 5: Electrochemical studies of moderately boron doped diamond in non aqueous electrolyte. *Electrochem. Appl. CVD Diam.* **2002**, 2–4.
34. Yuan, W.; Yuan, J.; Xie, J.; Li, C.M. Polymer-Mediated Self-Assembly of TiO<sub>2</sub>@Cu<sub>2</sub>O Core-Shell Nanowire Array for Highly Efficient Photoelectrochemical Water Oxidation. *ACS Appl. Mater. Interfaces* **2016**, *8*, 6082–6092. [[CrossRef](#)] [[PubMed](#)]

35. Shuang, S.; Lv, R.; Xie, Z.; Zhang, Z. Surface Plasmon Enhanced Photocatalysis of Au/Pt-decorated TiO<sub>2</sub> Nanopillar Arrays. *Sci. Rep.* **2016**, *6*, 26670. [[CrossRef](#)] [[PubMed](#)]
36. Tu, N.D.K.; Choi, J.; Park, C.R.; Kim, H. Remarkable Conversion between n- and p-Type Reduced Graphene Oxide on Varying the Thermal Annealing Temperature. *Chem. Mater.* **2015**, *27*, 7362–7369. [[CrossRef](#)]
37. Moniz, S.J.A.; Tang, J. Charge transfer and photocatalytic activity in CuO/TiO<sub>2</sub> nanoparticle heterojunctions synthesised through a rapid, one-pot, microwave solvothermal route. *ChemCatChem* **2015**, *7*, 1659–1667. [[CrossRef](#)]
38. Singh, P.; Nath, P.; Arun, R.K.; Mandal, S.; Chanda, N. Novel synthesis of a mixed Cu/CuO-reduced graphene oxide nanocomposite with enhanced peroxidase-like catalytic activity for easy detection of glutathione in solution and using a paper strip. *RSC Adv.* **2016**, *6*, 92729–92738. [[CrossRef](#)]
39. Chen, W.; Yan, L.; Bangal, P.R. Preparation of graphene by the rapid and mild thermal reduction of graphene oxide induced by microwaves. *Carbon N. Y.* **2010**, *48*, 1146–1152. [[CrossRef](#)]
40. Pei, S.; Cheng, H.M. The reduction of graphene oxide. *Carbon N. Y.* **2012**, *50*, 3210–3228. [[CrossRef](#)]



© 2018 by the authors. Licensee MDPI, Basel, Switzerland. This article is an open access article distributed under the terms and conditions of the Creative Commons Attribution (CC BY) license (<http://creativecommons.org/licenses/by/4.0/>).